mathematics

MDPI

Article

Numerical and Machine Learning Prediction of Blast and Fragment Propagation in RC Frames Under Internal Explosion

Tao Qiu and Junrun Li *

College of Civil Engineering, Tongji University, Shanghai 200092, China; 24310398@tongji.edu.cn
* Correspondence: 25310502@tongji.edu.cn; Tel.: +86-157-3504-4792

Abstract

Each component of reinforced concrete (RC) frames absorbs and dissipates blast energy, mitigating damage to adjacent rooms. Finite element modeling and machine learning are combined to analyze the propagation of blast waves and wall fragments in RC frames. A validated model simulates explosion scenarios with five TNT equivalents and examines blast loading and dynamic responses of adjacent rooms. Orthogonal experimental design is adopted to analyze the attenuation effects of structural parameters (room dimensions, venting coefficient, wall strength and thickness), TNT equivalent, and the number of propagation rooms on power parameters propagated to adjacent rooms. The results reveal that the peak overpressure and impulse of the adjacent rooms decrease by approximately two and one orders of magnitude, respectively, compared with the preceding room. The ejection velocity of wall fragments decays exponentially with the number of propagation rooms, which is the primary factor attenuating the power parameters, followed by the masonry wall strength and thickness. A backpropagation neural network-based surrogate model is developed to predict the attenuation coefficients of the power parameters (peak overpressure, duration, and wall fragment ejection velocity), achieving prediction errors below 20%. The proposed prediction framework provides a computationally efficient alternative to full-scale numerical simulation for rapid damage assessment.

Keywords: finite element modeling; machine learning; internal explosion; RC frame; blast wave; wall fragments

MSC: 68T07; 74S05; 76L05; 62K15

Check for updates

Academic Editor: Roman Ivanovich Parovik

Received: 16 September 2026
Revised: 13 October 2026
Accepted: 30 October 2026
Published: 6 November 2026

Copyright: © 2026 by the authors. Licensee MDPI, Basel, Switzerland. This article is an open access article distributed under the terms and conditions of the Creative Commons Attribution (CC BY) license.

1. Introduction

Reinforced concrete (RC) frame structures have been widely adopted due to their high load-bearing capacity, excellent seismic performance, and construction efficiency. Serving as critical facilities for wartime command and communication functions, these structures have become primary military targets in modern warfare [1,2]. For instance, in 2023, Russian forces employed hypersonic missiles to strike a Ukrainian command center, causing a progressive collapse of the RC frame and extensive damage [3]. Consequently, a thorough investigation of horizontal power propagation in RC frame structures under internal explosions can optimize pre-engagement weapon deployment and enable rapid post-blast damage assessment. Also, the findings can guide protective design for critical infrastructure.

Considerable research achievements have been made regarding the damage effects of conventional weapons in free-field and homogeneous media explosions, which could

address fundamental issues such as blast-resistant design of RC frame structures and munition design [4–6]. However, with the advancement of conventional weapons, significant improvements have been achieved in penetration capability, explosive power, and targeting accuracy, enabling incoming munitions to penetrate and detonate inside targets [7,8]. Under internal explosion, the blast wave propagation exhibits complex characteristics in RC frame structures. The masonry walls significantly attenuate the shock waves through energy absorption, and the failure of structural components consumes substantial explosive energy. These combined effects result in markedly reduced shock wave intensity when propagating to adjacent rooms, with the attenuation magnitude dependent on both structural and explosive parameters [9]. In recent years, several researchers have conducted systematic investigations on the blast load characteristics within single-room structures, while studies focusing on blast load characteristics in adjacent rooms remain relatively limited. Among these studies, Santos et al. [10] conducted full-scale internal explosion tests and numerical simulations on RC structures. Their results demonstrated that due to the attenuation of blast energy by masonry walls, the damage level of adjacent rooms was substantially lower than that of the explosive source room. Lopez et al. [11] carried out a series of explosion tests and numerical simulations on a two-bay full-scale RC frame structure, revealing that the directly impacted slab exhibited localized punching shear failure while the adjacent slab sustained only minor damage for 20 kg TNT. Guo et al. [12] conducted a series of internal explosion tests on a 1/3-scale RC structure with door and window openings to investigate the cumulative damage of the shear wall, though their study did not extend to analyzing the damage effects on adjacent rooms. Li et al. [13] conducted experimental research on the failure modes of multi-cabin structures under internal explosions, and their findings revealed a distinct cruciform ("+") pattern in the damage characteristics of multi-cabin structures. Liu [14] conducted internal explosion tests on a full-scale RC frame structure using two TNT charges (3 kg and 10 kg), demonstrating significant attenuation of overpressure and prolongation of duration in adjacent rooms. Lv et al. [15] carried out numerical simulations of internal explosions in a typical three-story prototype RC frame structure, with TNT equivalents ranging from 25 to 200 kg. They analyzed the propagation of blast shock waves inside the building structure and the resulting structural damage, and further established an efficient damage assessment method for building structures subjected to internal blast loading. Ou et al. [16] conducted internal explosion tests on a two-story prototype RC frame structure with infilled walls. The results revealed that load concentration effects arise at structural corners under internal blast loading, triggering overall punching shear failure of the infilled walls and floor slabs. Moreover, under the coupled action of shock wave loading and the impact of fragmented wall debris, the infilled walls and floor slabs in adjacent rooms along the propagation direction of the blast shock wave sustained more pronounced damage, corresponding to a higher overall damage level.

Compared to load-bearing RC components (i.e., beams, slabs, and columns), masonry walls exhibit larger load-bearing areas but weaker blast resistance. Under internal explosions, these walls are highly prone to collapse, causing damage to personnel and equipment within the structure while amplifying the scope of destruction [17,18]. Consequently, in addition to blast wave load, the damage assessment of adjacent rooms should account for the impact caused by wall ejection from the explosive source room [19]. The ejection velocity of wall fragments is difficult to measure experimentally due to sensor damage during wall collapse. Some researchers have focused on investigating the failure modes of masonry walls under blast load. Shi et al. [20] conducted close-in explosion tests on 240 mm-thick masonry walls, analyzing the characteristics of localized damage and wall fragments. Their results revealed that larger fragments accounted for a higher proportion and were concentrated near the wall. In contrast, smaller fragments, though less abundant,

exhibited higher initial velocities and were dispersed over greater distances. Yu et al. [21] conducted field blast tests on masonry walls using two TNT charges (3000 kg and 10,000 kg) at standoff distances of 70 m and 100 m, respectively, to investigate the dynamic response of masonry walls subjected to far-field blast load. The results demonstrated that the wall exhibited localized punching failure with fragments concentrated near the structure with 3000 kg TNT equivalent. In contrast, under the 10,000 kg TNT equivalent, the wall collapsed completely, and wall fragments were ejected approximately 3 m to 12 m away from the original location. Keys and Clubley [22], Ciornei [23], and Edri et al. [24] experimentally studied the dynamic response and fragment dispersion of masonry walls under uniformly distributed blast loads using large cross-section shock tubes. Their results identified three critical parameters influencing wall failure modes and fragment distribution: structural geometry, peak overpressure, and duration.

Generally, the existing studies still have the following main limitations: (i) the propagation of blast waves and load characteristics in adjacent rooms, especially the attenuation of shock waves by masonry walls, require further clarification [14]; (ii) the explosive ejection of failed wall fragments is a critical factor for assessing damage levels of adjacent rooms. However, research in this area remains relatively limited [20]; (iii) the influences of structural and blast parameters on attenuation of power parameters (i.e., peak overpressure, duration, ejection velocity of wall fragments) propagated to adjacent rooms have not been established systematically [22–24].

To address the above limitations, refined numerical studies on the internal explosion loads and dynamic behaviors of RC frame buildings are conducted. First, the applicability and effectiveness of the adopted FE analysis approach are validated through comparisons with existing test data from internal explosions on RC structures and close-in explosions on masonry walls, including material models and parameters, modeling methods, and fluid–structure interaction algorithms. Subsequently, for a typical RC frame building, the numerical simulation of internal explosions under TNT equivalents ranging from 20 to 500 kg is carried out to analyze the propagation of shock waves, load characteristics, and ejection velocity of wall fragments. Finally, based on the orthogonal tests and BP neural network, a predictive model is developed to calculate the attenuation coefficient of power parameters propagated to adjacent rooms across varying structural parameters, TNT equivalent, and number of propagation rooms. It should be noted that the numerical modeling methodology and its verification are described in detail in our previous work [25], in which the vertical propagation of power parameters in RC frame structures was investigated. The present study extends this methodology to the horizontal propagation of power parameters in a single-story multi-room RC frame. Therefore, only the modifications related to this horizontal propagation are presented in this paper.

2. FE Modeling and Analysis Approach

All numerical simulations in this study are performed using the explicit finite element code LS-DYNA. It is adopted because its well-developed ALE and Fluid–Structure interaction algorithms are well suited to strongly nonlinear problems such as blast wave propagation and large structural deformation, and its material library covers the constitutive models required in this work, namely concrete (K&C), masonry (RHT), and explosive (JWL), the parameters of which have been widely validated in blast and impact engineering applications.

2.1. FE Model

According to GB 50010-2010 "Code for Design of Concrete Structures" [26] and GB 50011-2010 "Code for Seismic Design of Buildings" [27], a typical single-story multi-

room RC frame was established, as shown in Figure 1. The single room measures 5000 mm × 5000 mm × 3000 mm; the RC columns and beams have cross-sectional dimensions of 500 mm × 500 mm and 250 mm × 500 mm, respectively; the slab thickness is 150 mm; and the window opening measures 900 mm × 2100 mm. The structure meets seismic fortification intensity level 7 and uses C40-grade concrete. The reinforcement details of each RC component are shown in Figure 1c–e. For the RC columns, the reinforcement consists of 12Φ25 (12 steel bars and a diameter of 25 mm) longitudinal bars and Φ8@100 stirrups (a diameter of 8 mm with a spacing of 100 mm). For the RC beam, the reinforcement consists of 6Φ22 (6 steel bars and a diameter of 22 mm) longitudinal bars and Φ8@100 stirrups (a diameter of 8 mm with a spacing of 100 mm). The slab is reinforced with two-way double layers of Φ10@150 longitudinal bars. The longitudinal bars and stirrups are constructed using HRB400 and HPB300 rebars, with a concrete cover thickness of 25 mm. The infill walls are built with clay brick, measuring 240 mm × 120 mm × 50 mm, and exhibiting a compressive strength of 10 MPa. TNT explosive is employed as the charge, with the detonation point positioned at the geometric center of the room. To accommodate a wide range of engineering scenarios, five TNT equivalents are selected: 20, 50, 100, 300, and 500 kg.

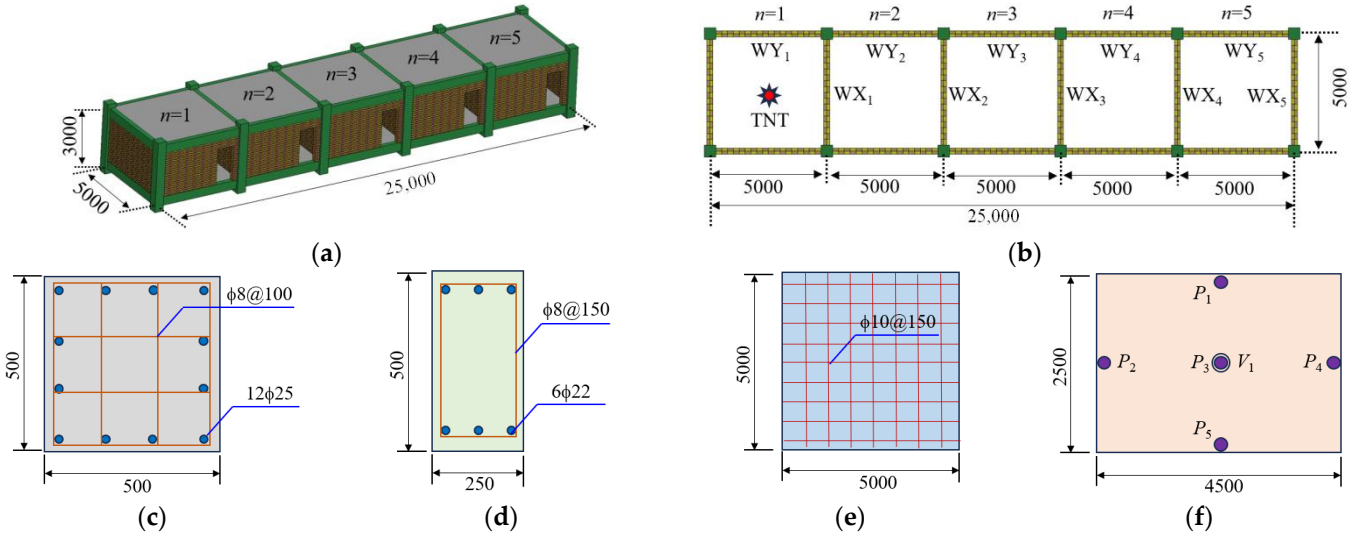


Figure 1. Structural dimensions and FE model, mm: (**a**) FE model of RC frame structure; (**b**) structural dimensions; (**c**–**e**) dimensions and reinforcement of RC columns, beams, and slabs; (**f**) layout of overpressure sensors and velocity sensors.

The mesh size adopted in this study was determined based on our previous work [28]. RC frame structure and masonry walls are modeled by Lagrange solid elements with a mesh size of 36 mm × 36 mm × 36 mm. Rebar is modeled using beam elements with a mesh size of 50 mm. Both the air and TNT are discretized via Arbitrary Lagrangian–Eulerian (ALE) elements. To prevent deviations in the numerical results caused by inconsistent air mesh sizes, the size is determined based on equivalent explosive mesh density [29]. Considering both structural dimensions and computational efficiency, a 2D–3D mapping method is employed to maintain adequate explosive mesh density for smaller TNT equivalents, while 3D finite element modeling is adopted directly for larger TNT equivalents.

2.2. Material Model and Parameters

The constitutive models adopted in this study are identical to those established and verified in our previous work [25], and they are briefly introduced below. The concrete is simulated by the K&C model (*MAT_CONCRETE_DAMAGE_REL3), which accounts for

both damage and strain rate effects, enabling accurate prediction of the dynamic response of concrete under high-strain-rate and large-deformation conditions. The material model and the strain rate effect of the rebar are described by the *MAT_PLASTIC_KINEMATIC model and the Cowper–Symonds (CS) model, respectively. For the masonry walls, a simplified microscopic method is adopted. The mortar thickness is incorporated within expanded brick elements that integrate both the brick units and the adjacent mortar joints, and cohesive contact modeling between the expanded brick elements is employed to characterize the bonding effect of the mortar, enabling the simulation of brick–mortar interaction with enhanced computational efficiency. The expanded brick units are simulated by the *RHT (Riedel–Hiermaier–Thoma) model, which accounts for material failure, damage, hardening, and strain rate effects, making it suitable for capturing the dynamic behavior of masonry walls under high pressure and high strain rates. The propagation of blast waves and their interaction with the RC structure are realized via the ALE algorithm coupled with the FSI (fluid–structure interaction) method. The detonation process of the TNT explosive and the compression behavior of the detonation products are described by the *MAT_HIGH_EXPLOSIVE_BURN material model and the *EOS_JWL equation of state, and air is regarded as a non-viscous ideal gas modeled by *MAT_NULL. The detailed formulations and calibrated parameters are presented in our previous work [25].

2.3. Verification of Finite Element Method

The reliability of the numerical model is validated via two approaches: comparison of overpressure–time histories against the internal blast tests on RC frames (Liu [14]), and comparison of damage patterns and damage areas against the close-in blast tests on masonry walls (Shi et al. [20]). As damage patterns and damage areas reflect the wall failure mode and the fragment generation process, these comparisons provide indirect corroboration for the rationality of the fragment ejection behavior. With respect to direct validation of the ejection velocity of wall fragments, the available literature currently contains extremely limited measured data regarding the flight velocity of masonry fragments under internal blast conditions. Furthermore, significant discrepancies exist across existing tests in terms of charge mass, wall configuration, and sensor layout, which renders it challenging to acquire quantitative data directly comparable to the working conditions investigated in this study. Accordingly, direct validation of the fragment ejection velocity is not conducted in the current study.

2.3.1. Explosion Test in RC Frame Structures

As shown in Figure 2a, Liu [14] conducted an experimental study on a single-story, single-bay, two-span, full-scale RC frame structure with window openings. The individual room measured 4200 mm × 6000 mm × 3600 mm, with all walls constructed using AAC masonry. The masonry walls consisted of AAC blocks (600 mm × 240 mm × 240 mm) bonded with 10 mm cement mortar. A window opening (1800 mm × 1800 mm) was incorporated in the shorter span. The concrete had a compressive strength of 35 MPa, while the AAC blocks and mortar exhibited compressive strengths of 3.5 MPa and 10 MPa, respectively. Detailed component dimensions and reinforcement layout can be found in the referenced literature [14]. Two internal explosion tests were conducted with 3 kg and 10 kg TNT equivalents, respectively. The finite element model is shown in Figure 2b,c. Air mesh sizes are determined based on equivalent explosive mesh density [29], as shown in Table 1.

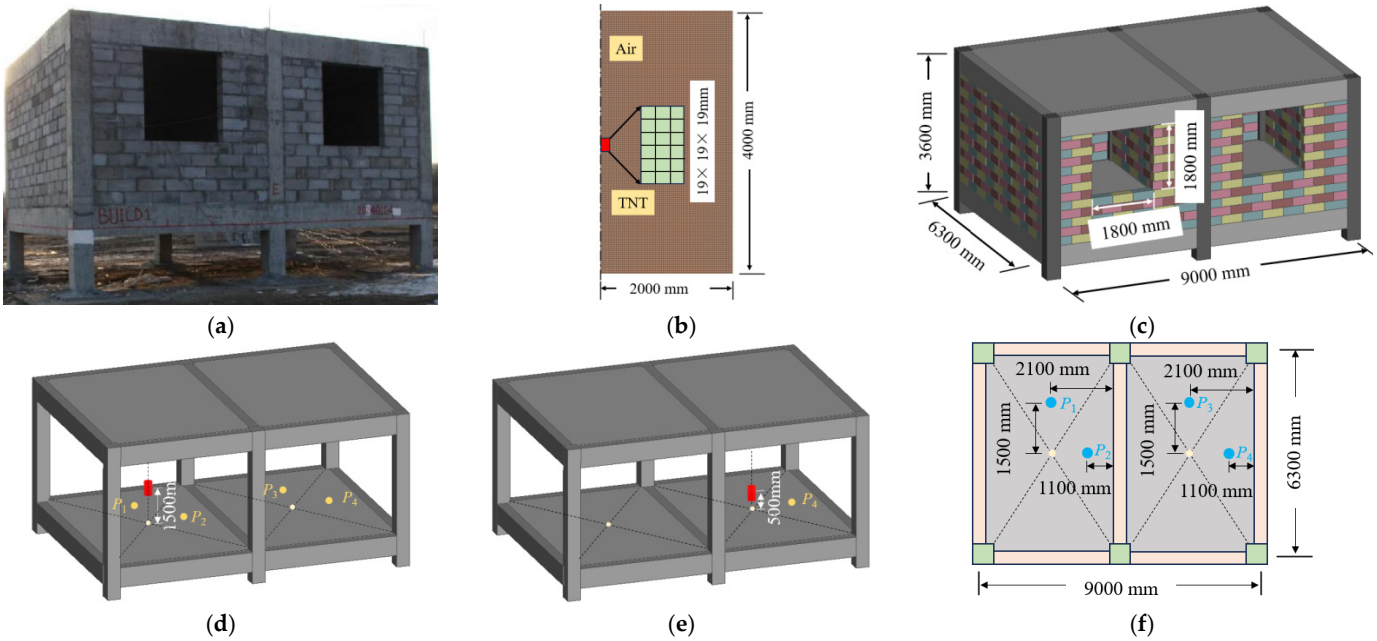


Figure 2. Internal explosion tests on RC structure and corresponding FE model: (**a**) test room [14]; (**b**) 2D finite element model; (**c**) 3D finite element model; (**d**) explosive location, Test-1; (**e**) explosive location, Test-2; (**f**) layout of overpressure sensors.

Table 1. Mesh sizes of the FE model for each explosion scenario.

Test No.		TNT Equivalents (kg)	Equivalent Explosive Mesh Density [29]	2D Finite Element Model		3D Finite Element Model	
				TNT Mesh (mm)	Air Mesh (mm)	TNT Mesh (mm)	Air Mesh and Structure Mesh (mm)
Liu [14]	Test-1	3.0	255.8	122 × 122	19 × 19	/	36 × 36 × 36
	Test-2	10.0	255.8	/	/	182 × 182 × 182	36 × 36 × 36
Shi et al. [20]	Test-3	1.0	255.8	84.9 × 84.9	13.4 × 13.4	/	36 × 36 × 36
	Test-4	6.0	255.8	/	/	154 × 154 × 154	36 × 36× 36

Figure 3 shows the overpressure–time history curves at different measurement points for two TNT equivalents. The results demonstrate that internal blast load in confined spaces exhibits multi-peak characteristics. The simulated overpressure–time history curves show good agreement with test data in terms of variation trends, with peak overpressure deviations within 15%. Further analysis of the shock wave propagation under 3 kg TNT (Test-1) was conducted. Figure 4 shows the dynamic pressure distribution inside the structure at different time intervals. At T = 0.8–5 ms, the shock wave penetrated the wall and propagated into Room 2 with significantly reduced peak overpressure compared with Room 1. At T = 10–20 ms, the pressure in Room 2 gradually increased as the shock waves propagated, reaching maximum pressure at measurement points P_2 and P_3. At T = 30–50 ms, multiple reflections between Rooms 1 and 2 led to multi-peak features in the overpressure–time history curves. At T = 80–100 ms, quasi-static pressure was formed in Room 2, while the internal pressure in Room 1 gradually dissipated due to wall failure.

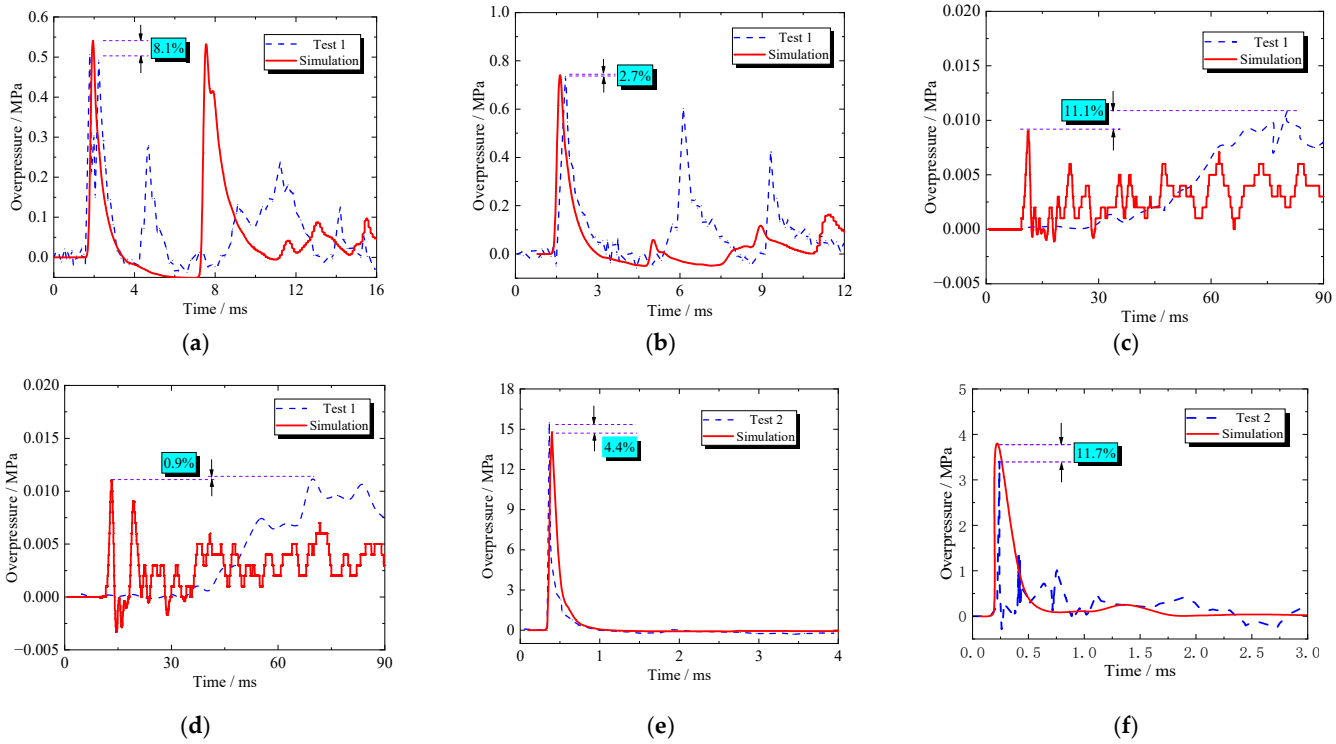


Figure 3. Comparisons of test and simulated overpressure–time histories: (**a**–**d**) measurement point P_1–P_4, Test-1; (**e**) measurement point P_1, Test-2; (**f**) measurement point P_4, Test-2.

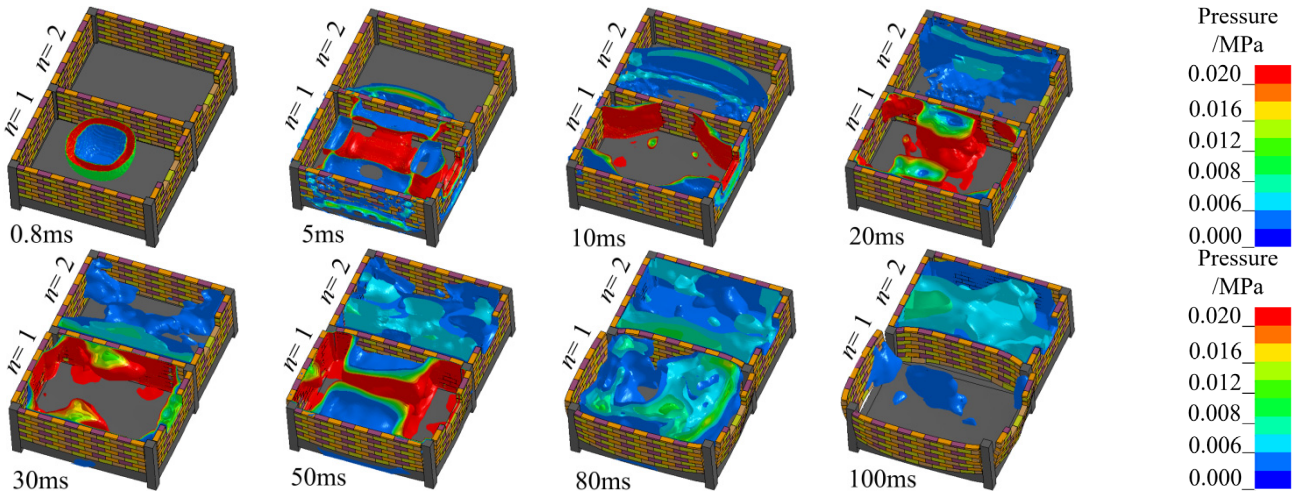


Figure 4. Dynamic pressure distribution inside the RC frame structure (Test-1).

2.3.2. Close-In Explosions on Masonry Walls

The close-in explosion tests on masonry walls conducted by Shi et al. [20] are identical to those used for validation in our previous work [25]. Table 2 summarizes the validation errors, including a comparison of the tested and simulated damage areas of the masonry walls, showing that the errors in the damage areas are less than 20%. The detailed validation procedures and results are presented in our previous work [25].

This section verifies the reliability of the FE modeling by comparing the simulated overpressure–time histories, shock wave propagation, and structural damage with those measured in the internal explosion tests on RC frame buildings and the close-in explosion tests on masonry walls.

Table 2. Comparison of tests and simulated damage areas of masonry walls.

Parameters	1 kg TNT		6 kg TNT	
	Blast-Facing Surface	**Back-Blast Surface**	**Blast-Facing Surface**	**Back-Blast Surface**
Simulation	320 mm × 180 mm	400 mm × 300 mm	520 mm × 560 mm	900 mm × 900 mm
Test	370 mm × 190 mm	360 mm × 330 mm	500 mm × 500 mm	920 mm × 930 mm
Error	−18.1%	1.0%	16.5%	−5.33%

3. Results and Analysis

3.1. Blast Wave Propagation

Taking the 100 kg TNT equivalent as an example, Figure 5 shows the dynamic pressure distribution in the RC structure at different time intervals. At T = 2 ms, shock waves generated in Room 1 impacted the structural components (i.e., RC columns, RC beams, and RC slabs) and masonry walls, producing reflected overpressures. At T = 20 ms, internal pressure in Room 1 exhibited significant decay concomitant with global shear failure and subsequent ejection of the surrounding masonry walls. Concurrently, the blast wave propagated into Room 2, revealing the progressive failure mode observed in confined explosion environments. At T = 40 ms, internal pressure in Room 1 dissipated due to venting effects through the failed RC slab and walls, while Room 2 formed quasi-static pressure. At T = 60 ms, internal pressure in Room 2 concentrated near the masonry wall WX_2 as the failed wall WX_1 moved inward, creating localized pressure increases. At T = 100 ms, the pressure in Room 2 completely dissipated, with only residual shock waves propagating into Room 3. However, the energy absorption by walls WX_1/WX_2 and structural venting reduced the internal pressure in Room 3 to atmospheric level.

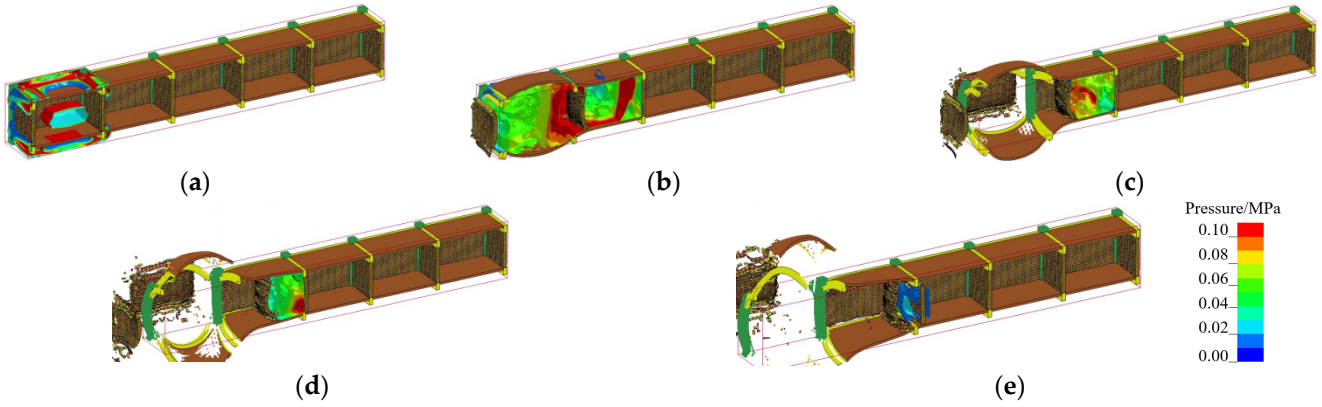


Figure 5. Dynamic pressure distribution of blast waves: (**a**) T = 2 ms; (**b**) T = 20 ms; (**c**) T = 40 ms; (**d**) T = 60 ms; (**e**) T = 100 ms.

3.2. Load Characteristics in Adjacent Rooms

The load characteristics of feature points can be effectively utilized for rapid damage assessment and blast-resistant design of structures. This section systematically analyzes the load characteristics at both wall center and corner points under various scenarios, while specifically investigating the blast loads in adjacent rooms. The pressure measurement points are shown in Figure 1f, ensuring comprehensive monitoring of dynamic pressure distribution during explosive events.

Taking the 100 kg TNT equivalent as an example, Figure 6 shows the overpressure–time and impulse–time history curves at measurement points in Rooms 1–3. Since the internal pressures in Rooms 4 and 5 remain at near-atmospheric levels, the damage to the

structure is negligible. As shown in Figure 6a,d, the blast load in the explosive source room (Room 1) exhibits complex multi-peak characteristics. The corner convergence effect causes considerable variation in maximum overpressure among different measurement points (maximum deviation: 56.3%), while the impulses remain relatively consistent (maximum deviation: 15%). Figure 6b,c,e,f reveal that Rooms 2 and 3 experience gradual pressure buildup, forming quasi-static pressures with relatively low overpressure but prolonged durations. For a given wall type (WX or WY) within adjacent rooms, the overpressure–time and impulse–time history curves exhibit similar profiles, with maximum deviations below 10% in both peak overpressure and impulse. Furthermore, the average maximum overpressure and impulse differences between WX-type and WY-type walls remain within 15%. For instance, the average peak overpressures of WX_2 and WY_2 walls are 0.12 MPa and 0.11 MPa, and the maximum impulses are 4.1 MPa·ms and 3.5 MPa·ms, respectively, all showing less than 15% variation. These findings confirm that load characteristics at the wall center can be used to characterize the blast loads in adjacent rooms for subsequent studies.

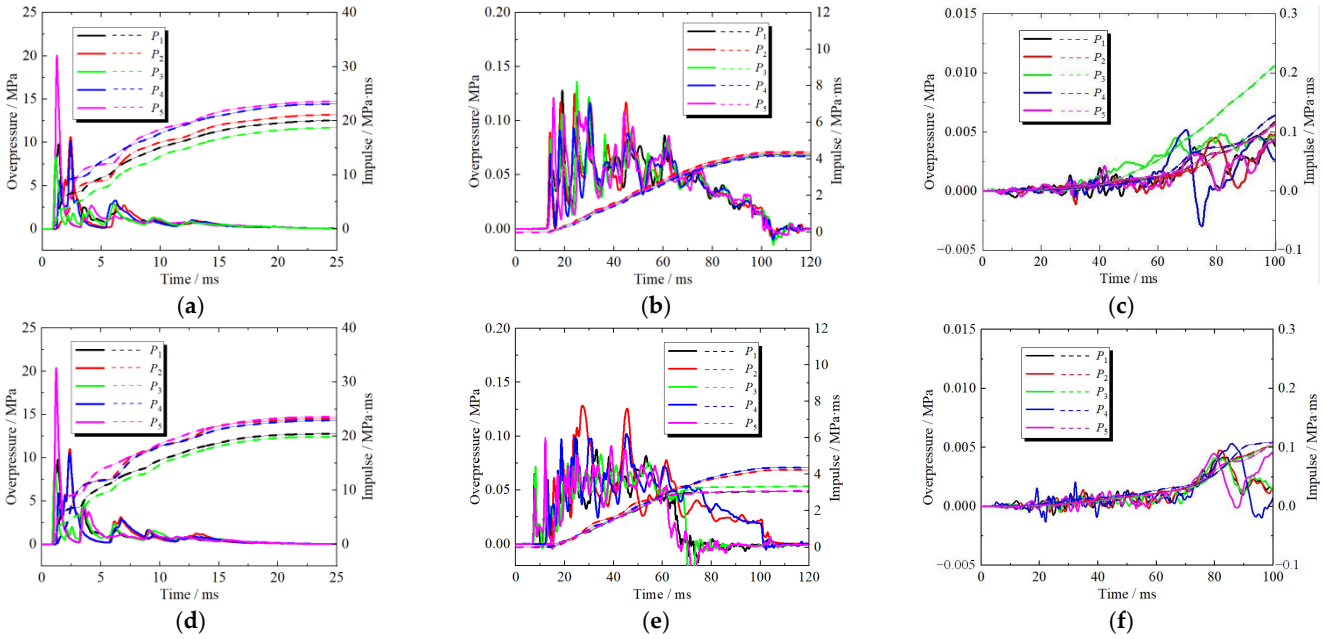


Figure 6. Overpressure–time and impulse–time histories with 100 kg TNT: (**a**) WX_1, $n = 1$; (**b**) WX_2, $n = 2$; (**c**) WX_3, $n = 3$; (**d**) WY_1, $n = 1$; (**e**) WY_2, $n = 2$; (**f**) WY_3, $n = 3$. Note: the measurement points P_1–P_5 are shown in Figure 1f; WX and WY denote the walls parallel and perpendicular to the shock wave propagation direction, respectively, and n is the number of propagation rooms.

To quantitatively evaluate the attenuation effect of shock waves by masonry walls, Figure 7a shows the overpressure–time and impulse–time history curves at the center of WX_1, WX_2, and WX_3 walls with 100 kg TNT. The peak overpressure $P_{n=2}$ and impulse $I_{n=2}$ in Room 2 are 0.26 MPa and 4.56 MPa·ms, representing approximately 1.3% and 19.6% of the values in the explosive source room ($P_{n=1}$ = 20.0 MPa, $I_{n=1}$ = 23.2 MPa·ms). Similarly, the peak overpressure $P_{n=3}$ and impulse $I_{n=3}$ in Room 3 are 0.0048 MPa and 0.21 MPa·ms, representing approximately 0.02% and 1% of the values in the explosive source room. Therefore, each penetration of a wall by the blast wave reduces peak overpressure by approximately two orders of magnitude and impulse by one order of magnitude, demonstrating the substantial energy absorption capacity of masonry walls. Consistently, the internal explosion tests on RC frame structures conducted by Guo et al. [30] re-

vealed similar attenuation characteristics, further corroborating the reliability of the present numerical approach.

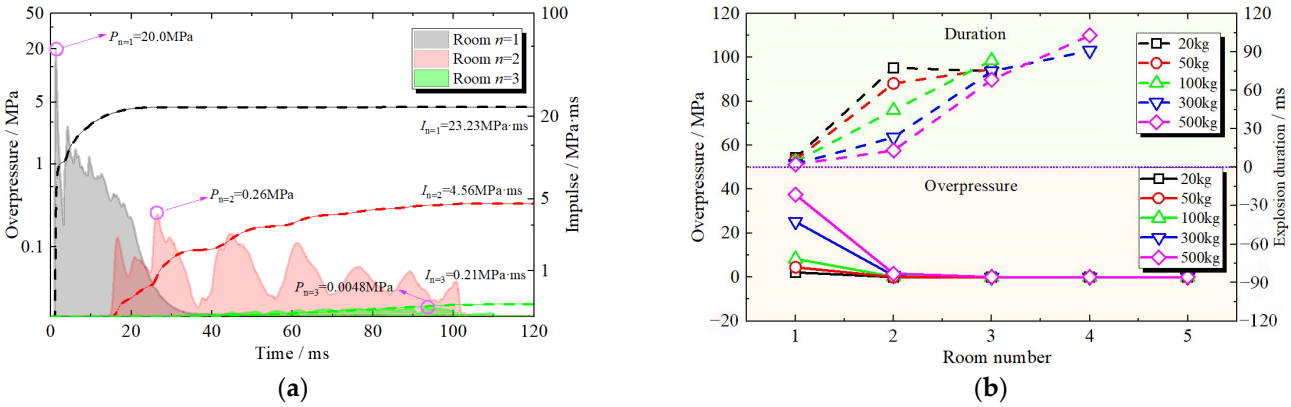


Figure 7. Load characteristics in adjacent rooms: (**a**) overpressure–time and impulse–time history curves with 100 kg TNT; (**b**) peak overpressure and equivalent duration in each scenario.

Furthermore, to determine the equivalent duration in adjacent rooms, the overpressure–time history curves are idealized as triangular pulses. This idealization is a standard procedure in the engineering treatment of blast loads, and has been widely adopted in blast-resistant design codes including the UFC 3-340-02 [31].

Based on impulse equivalence principles, the equivalent duration t_d is calculated by $t_d = 2I/P$ (where I and P are impulse and peak overpressure, respectively). This simplified approach establishes a fundamental basis for rapid damage assessment on RC frame structures under internal explosions. Figure 7b shows the peak overpressure and equivalent duration in each room. The results demonstrate that peak overpressure decreases approximately exponentially with the number of propagation rooms, whereas the equivalent duration is governed by the relative attenuation of peak overpressure and impulse. For 500 kg TNT, the peak overpressure and equivalent duration in Room 2 are 1.59 MPa and 13.1 ms, representing approximately 95.8% reductions and 396.2% increases, respectively, compared with the center of wall WX1 (37.54 MPa, 2.64 ms). These findings quantitatively confirm the significant attenuation effect of shock waves by masonry walls.

3.3. Structural Failure Mode

In RC frame structures, masonry walls serve as critical components for dividing horizontal space, protecting adjacent rooms by mitigating shock wave propagation and fire spread. Compared to RC components (i.e., columns, beams, and slabs), masonry walls exhibit lower strength and structural integrity, making them more susceptible to damage under internal explosion. Thus, when analyzing failure modes in adjacent rooms, the damage to primary RC components can be neglected, with a focus on the dynamic behavior of masonry walls. Figures 8 and 9 show the horizontal failure process of the RC frame structure subjected to internal explosions.

For the 20 kg TNT equivalent: at T = 50 ms, four masonry walls in the source room (Room 1) experienced global shear failure and were ejected. At T = 100–200 ms, wall WX1 continued moving along the propagation direction of shock waves, while wall WX2 showed negligible lateral displacement. This observation confirms that the attenuated shock wave in Room 2 caused minor damage to wall WX2. As established in Section 3.2, Room 2 formed quasi-static pressure, while masonry wall WY2 exhibited minor displacement. This damage likely resulted from flexural deformation of the surrounding RC columns and beams, which induced compressive failure in the wall. At T = 300 ms, wall WX2 experienced complete

collapse due to impact from failed wall WX1. At T = 500–900 ms, wall WX3 sustained minor damage under successive impacts from wall WX1 and WX2, with significant brick fragment accumulation in Room 3.

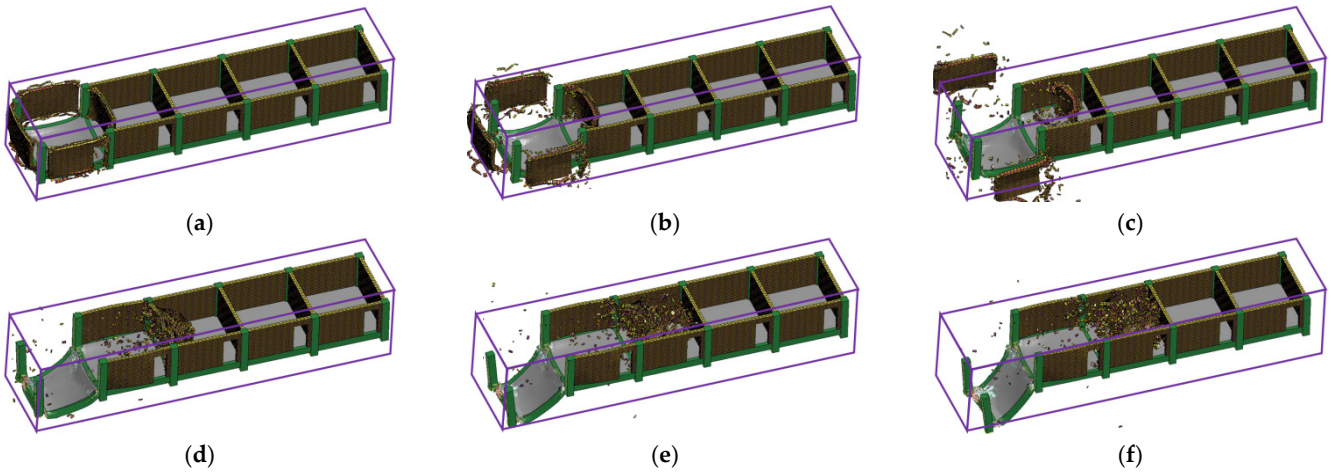


Figure 8. Failure process of RC frame structure with 20 kg TNT: (**a**–**f**) T = 50, 100, 200, 300, 500, and 900 ms.

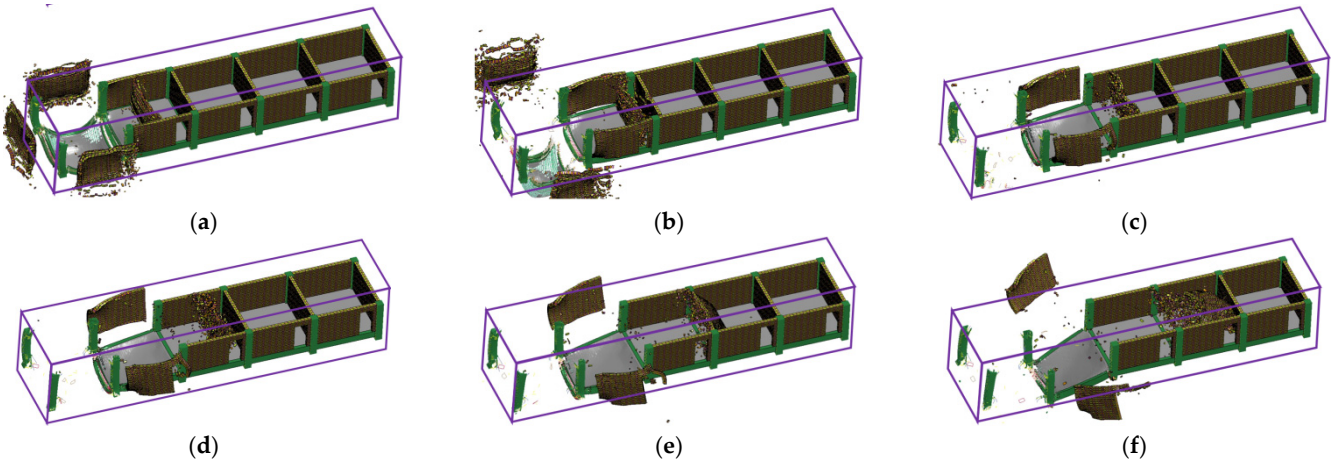


Figure 9. Failure process of RC frame structure with 100 kg TNT: (**a**–**f**) T = 50, 100, 200, 300, 500, and 900 ms.

For the 100 kg TNT equivalent: at T = 50 ms, four masonry walls in the source room (Room 1) experienced global shear failure and were ejected. At T = 100 ms, masonry walls WX2 and WY2 had experienced global shear failure due to shock waves, though WX2 had not yet been subjected to impact from the failed WX1 wall. At T = 200–300 ms, masonry walls WX2 and WX1 moved along the propagation direction of shock waves, while walls WY3 and WX3 showed negligible displacement. This observation confirms minimal damage to the masonry wall by shock waves propagated into Room 3. At T = 500 ms, wall WX3 completely collapsed due to the impact from WX1 and WX2, continuing its movement along the propagation direction of shock waves. At T = 900 ms, wall WX4 sustained minor damage through sequential impacts from WX1-WX3, resulting in significant brick fragment accumulation in Room 4.

The distinct damage mechanisms of structural failure modes are revealed through a comparative analysis under 20 kg and 100 kg TNT. For smaller TNT equivalents (e.g., 20 kg TNT), the shock wave propagating to adjacent rooms causes minimal damage to masonry walls. The primary mechanism inducing masonry wall failure is the impact from failed

walls in the explosive source room. For larger TNT equivalents (e.g., 100 kg TNT), the damage assessment of masonry walls in adjacent rooms must account for both the shock waves and impact from failed walls. Therefore, the shock waves should be adopted as the sole evaluation parameter for assessing damage on WY-type walls. Given the complexity of internal blast load and diverse failure modes of masonry walls, the kinetic energy ($E = 1/2Mv^2$) of masonry walls is adopted to characterize the dynamic response of WX-type walls. Assuming a constant wall mass (M), the ejection velocity at the wall center (see Figure 1f) can be used as a proxy for kinetic energy.

Figure 10 shows the velocity–time histories measured at the centers of masonry walls under 20 kg and 100 kg TNT equivalents, respectively. For 20 kg TNT equivalent: at T = 300 ms, wall WX1 impacted WX2, causing $V_{n=1}$ to decrease from 18.5 m/s to 7.1 m/s. Meanwhile, wall WX2 acquired initial kinetic energy, and $V_{n=2}$ = 10.8 m/s. At T = 800 ms, wall WX2 impacted WX3, resulting in $V_{n=2}$ dropping to 0 m/s. At T = 1050 ms, wall WX1 impacted WX3, and $V_{n=1}$ decreased to 0 m/s, marking the end of the failure process. $V_{n=3}$ < 1.0 m/s indicated that wall WX3 had not experienced bending damage and had sustained only minimal damage. For 100 kg TNT equivalent: at T = 150 ms, wall WX1 impacted WX2, causing $V_{n=1}$ to decrease from 40 m/s to 17.5 m/s. Meanwhile, wall WX2 acquired initial kinetic energy, and $V_{n=2}$ = 17.8 m/s. At T = 400 ms, walls WX1 and WX2 impacted WX3, causing $V_{n=2}$ to decrease from 17.8 m/s to 9.6 m/s, while wall WX3 acquired initial kinetic energy and $V_{n=3}$ = 9.6 m/s. At T = 1000 ms, walls WX1, WX2, and WX3 collided with WX4, causing $V_{n=3}$ to decrease from 6.7 m/s to 1.2 m/s, while wall WX4 acquired initial kinetic energy and $V_{n=4}$ = 1.2 m/s. At T = 1100 ms, the four masonry walls continued to move forward at the same speed, marking the end of the failure process. Notably, before the impact between walls WX1 and WX2, wall WX2 had already attained an initial velocity of $V_{n=2}$ = 8.7 m/s due to the shock wave load. This indicates that the shock wave propagating into Room 2 caused significant damage to wall WX2, consistent with the results of the structural failure process.

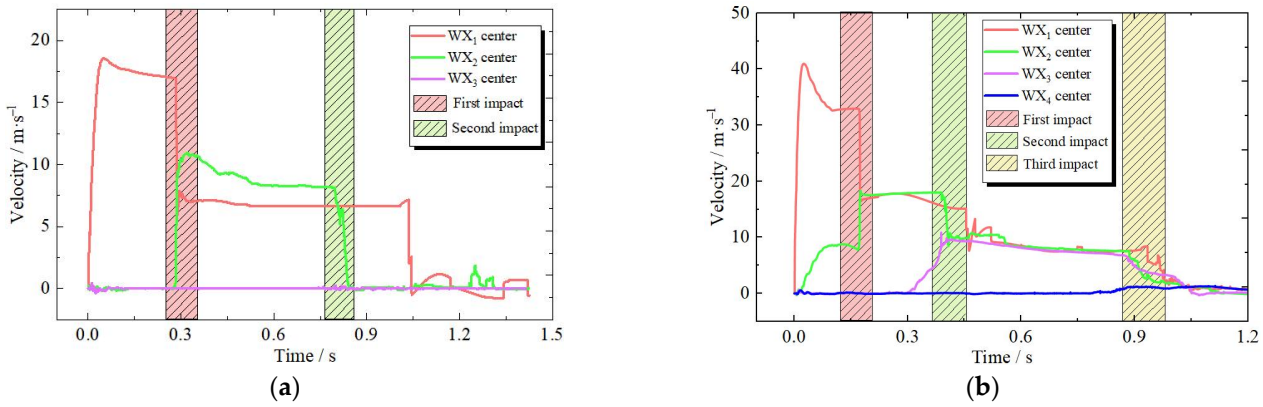


Figure 10. Velocity–time history curves of wall center: (**a**) 20 kg TNT; (**b**) 100 kg TNT.

In summary, the ejection velocity at the wall center can effectively characterize the dynamic behavior of masonry walls and can serve as a key input parameter for assessing damage on WX-type walls in adjacent rooms. It should be noted that, although the wall center velocity alone is insufficient to capture the size, morphology, and spatial distribution of wall fragments, and the velocity and mass distributions of masonry fragments are highly non-uniform in practical scenarios, this characterization remains justified for the blast scenarios investigated in this study. For such scenarios, the masonry wall undergoes global shear failure under blast loading and is ejected as an integrated whole, approximately behaving as a rigid body in translational motion; accordingly, the wall center velocity can

adequately represent the overall motion and total kinetic energy of the wall. Moreover, as an input parameter for the rapid damage assessment and prediction model of adjacent rooms, it provides a unified and comparable metric, which is corroborated by the numerically predicted damage patterns. Nevertheless, its inherent limitations should be fully considered when the characterization is extended to other failure modes or fragment-level assessments.

4. Prediction Model of Power Attenuation Coefficient

4.1. Analysis of Influencing Factors

As indicated in Section 3, under internal explosion, the damage to WY-type walls is solely related to the shock waves and can be characterized by the peak overpressure (P) and equivalent duration (t). Similarly, the damage to WX-type walls requires considering both the shock waves and the impact from the failed walls in the explosive source room, which can be characterized by the ejection velocity (V) of the wall center. Therefore, the main power parameters in adjacent rooms include the peak overpressure (P), duration (t), and ejection velocity (V) of the wall center.

Assuming that the explosive is detonated at the room center, the influence factors affecting the power parameters in adjacent rooms include the explosive equivalent (W), room length (R), venting coefficient $(S/V^{2/3})$, number of propagation rooms (n), as well as the strength (σ) and thickness (H) of masonry walls, as shown in Figure 11. To ensure that the established prediction model fits most engineering scenarios, the explosive weight is set to: 20, 50, 100, 300, and 500 kg; the room length is set to: 3, 5, 8, and 10 m; the venting coefficient is set to: 0.2, 0.4, 0.6, 0.8, and 1.0; n is set to: 1, 2, 3, 4, and 5; the strength of masonry walls is set to: 5, 10, 15, and 20 MPa; the thickness of masonry walls is set to: 120, 180, and 240 mm. Given that full factorial simulations need substantial resources and time, orthogonal tests are employed to determine the simulation conditions, as shown in Table 3. Specifically, the L25 orthogonal array was adopted to arrange the 25 simulation cases. Since several factors are restricted to 4 or 3 levels by practical engineering constraints (room length: 3, 5, 8, and 10 m; wall strength: 5, 10, 15, and 20 MPa; wall thickness: 120, 180, and 240 mm), a mixed-level design was implemented through level merging in the standard five-level orthogonal table. All factor levels were determined in accordance with practical engineering conditions and the parameter range reported in the existing literature, so as to cover a wide spectrum of realistic scenarios.

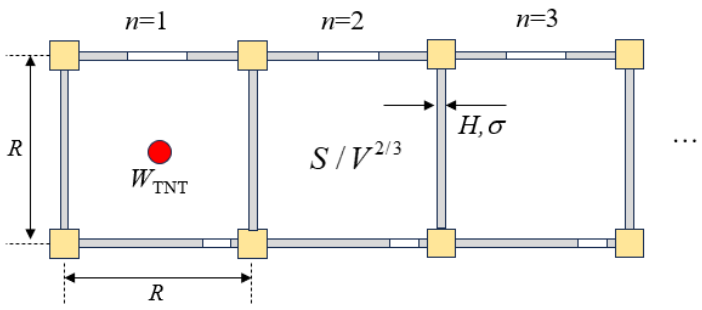


Figure 11. Influence factors of power parameters. Note: W is TNT equivalent, R is room dimension, $S/V^{2/3}$ is venting coefficient, n is the number of propagation rooms, σ and H are the strength and thickness of masonry walls, respectively.

Table 3. Orthogonal test design and attenuation coefficients.

Scenario	Factors						Parameters		
	IF1	*IF2*	*IF3*	*IF4*	*IF5*	*IF6*	η_1	η_2	φ
1	20	3	1	1	5	240	0.00	0.00	0.00
2	50	5	0.6	4	5	180	1.00	1.00	1.00
3	100	8	0.2	2	20	120	0.99	0.86	0.50
4	300	10	0.8	5	15	240	1.00	1.00	1.00
5	500	3	0.4	3	10	120	1.00	0.99	0.67
6	20	3	0.2	4	15	180	1.00	1.00	0.93
7	50	5	0.8	2	10	240	0.99	0.76	0.62
8	100	8	0.4	5	5	180	1.00	1.00	1.00
9	300	10	1	3	10	120	1.00	1.00	0.88
10	500	5	0.6	1	20	180	0.00	0.00	0.00
11	20	3	0.4	2	15	120	0.94	0.80	0.45
12	50	5	1	5	20	240	1.00	1.00	1.00
13	100	8	0.6	3	15	240	1.00	0.99	0.96
14	20	10	0.2	1	10	180	1.00	1.00	0.86
15	50	8	0.8	4	5	120	1.00	1.00	0.85
16	100	3	0.6	5	10	120	1.00	0.96	0.77
17	300	5	0.2	3	5	240	0.00	0.00	0.00
18	500	8	0.8	1	20	120	1.00	1.00	0.95
19	20	10	0.4	4	20	240	1.00	0.91	0.45
20	50	10	1	2	15	180	1.00	0.95	0.79
21	100	3	0.8	3	20	180	0.00	0.00	0.00
22	300	5	0.4	1	15	120	1.00	1.00	0.82
23	500	8	1	4	10	180	0.99	0.88	0.53
24	20	10	0.6	2	5	180	1.00	1.00	0.91
25	50	5	0.2	5	10	240	1.00	1.00	0.86

Note: *IF1*–*IF6* are TNT weight, room length, venting coefficient, number of propagation rooms, wall strength and thickness, respectively; η_1, η_2 and φ are the attenuation coefficients of peak overpressure, equivalent duration, and ejection velocity of wall center, respectively.

To investigate the attenuation of power parameters propagated to adjacent rooms by each influencing factor, attenuation coefficients for peak overpressure, equivalent duration, and ejection velocity of the wall center are defined, as shown in Equations (1)–(3). The calculated results are listed in Table 3. When the peak overpressure is below 0.01 MPa, the damage to human tissue is negligible. To guarantee the stability of subsequent statistical analysis and modeling, the peak overpressure of such cases is recorded as 0 MPa, with an equivalent duration set to 1000 ms, so as to avoid numerical anomalies caused by undefined equivalent duration when the peak overpressure approaches zero. In addition, this processing drives the attenuation coefficients of these cases toward boundary values (approaching 0 or 1), leading to boundary clustering within the sample set. Nevertheless, such cases exclusively occur in scenarios with a large number of propagation rooms, where the blast load has already decayed to a negligible level, and only account for a limited proportion of the total samples. Accordingly, this treatment neither alters the core conclusion of the statistical analysis that the number of propagation rooms is the dominant influencing factor, nor exerts a significant impact on the prediction performance of the machine learning model.

$$\eta_1 = P_n/P_1 \tag{1}$$

$$\eta_2 = (t_n - t_1)/t_n \tag{2}$$

$$\varphi = v_n/v_1 \tag{3}$$

where η_1, η_2, and φ are the attenuation coefficients of peak overpressure, equivalent duration, and ejection velocity of the wall center; P_n, t_n, and v_n are the peak overpressure, equivalent duration, and ejection velocity of the wall center in the n-th room; P_1, t_1, and v_1 are the peak overpressure, equivalent duration, and ejection velocity of the wall center in the explosive source room.

4.2. Significance Analysis

Range analysis is a straightforward method for assessing the influence of different factors on experimental results [32]. The influence of each factor on the results can be determined by comparing their ranges in orthogonal experiments. Range analysis was conducted on the explosive equivalent (W), room length (R), venting coefficient $(S/V^{2/3})$, number of propagation rooms (n), strength (σ) and thickness (H) of masonry walls to determine their influence on the attenuation coefficient of power parameters and to establish their order of significance. The calculation principle for the k values follows Equation (4), and the calculation results are listed in Table 4.

$$k_i = \left[max\left(\overline{y}_{i1}, \overline{y}_{i2}, \cdots, \overline{y}_{ij}\right) - min\left(\overline{y}_{i1}, \overline{y}_{i2}, \cdots, \overline{y}_{ij}\right)\right]/N \quad (4)$$

where k_i is the range of factor i; $\overline{y}_{ij}$ is the average value of factor i at level j; N is the number of simulations.

Table 4. Range analysis.

Parameters	*IF1*	*IF2*	*IF3*	*IF4*	*IF5*	*IF6*
Attenuation coefficients of peak overpressure						
K_1	0.80	0.82	0.80	0.00	0.83	0.74
K_2	0.80	0.71	0.80	0.98	0.86	0.78
K_3	0.80	0.83	0.79	1.00	0.82	0.87
K_4	0.80	0.83	0.79	1.00	0.66	/
K_5	0.80	/	0.79	1.00	/	/
k	0.00	0.12	0.01	1.00	0.20	0.13
Attenuation coefficients of equivalent duration						
K_1	0.77	0.79	0.78	0.00	0.80	0.71
K_2	0.75	0.67	0.74	0.84	0.82	0.75
K_3	0.76	0.81	0.77	0.98	0.78	0.84
K_4	0.77	0.80	0.76	1.00	0.63	/
K_5	0.76	/	0.76	1.00	/	/
k	0.02	0.14	0.04	1.00	0.19	0.13
Attenuation coefficients of ejection velocity at the wall center						
K_1	0.63	0.62	0.63	0.00	0.69	0.53
K_2	0.69	0.61	0.65	0.51	0.68	0.61
K_3	0.66	0.69	0.67	0.81	0.63	0.78
K_4	0.60	0.63	0.61	0.91	0.54	/
K_5	0.61	/	0.62	0.95	/	/
k	0.08	0.08	0.06	0.95	0.15	0.25

Note: K_1–K_5 are the average attenuation coefficients of power parameters at the same level; k is the range for each influencing factor.

Figure 12 shows the range radar charts of the influence factors on attenuation coefficients of peak overpressure, equivalent duration, and ejection velocity of wall center. The ranges of six factors on the coefficient η_1 are 0.00, 0.12, 0.01, 1.00, 0.20, and 0.13, respectively. Among them, the factor with the largest range is the number of propagation rooms (n), indicating that it has the most significant impact on the attenuation coefficient of peak overpressure (η_1). Their significance on the coefficient η_1 follows this descending order: $n > \sigma > H > R > S/V^{2/3} > W$. The ranges of six factors on the coefficient η_2 are 0.02, 0.14, 0.04, 1.00, 0.19, and 0.13, respectively. Their significance on the coefficient η_2 follows this descending order: $n > \sigma > R > H > S/V^{2/3} > W$. The ranges of the six factors on the coefficient φ are 0.08, 0.08, 0.06, 0.95, 0.15, and 0.25, respectively. Their significance on the coefficient η_2 follows this descending order: $n > H > \sigma > R = W > S/V^{2/3}$. By analyzing the k values

of wall strength and thickness at different factor levels, it can be found that increasing the strength and thickness of masonry walls can effectively reduce the shock wave load and the ejection velocity of wall fragments propagated to adjacent rooms.

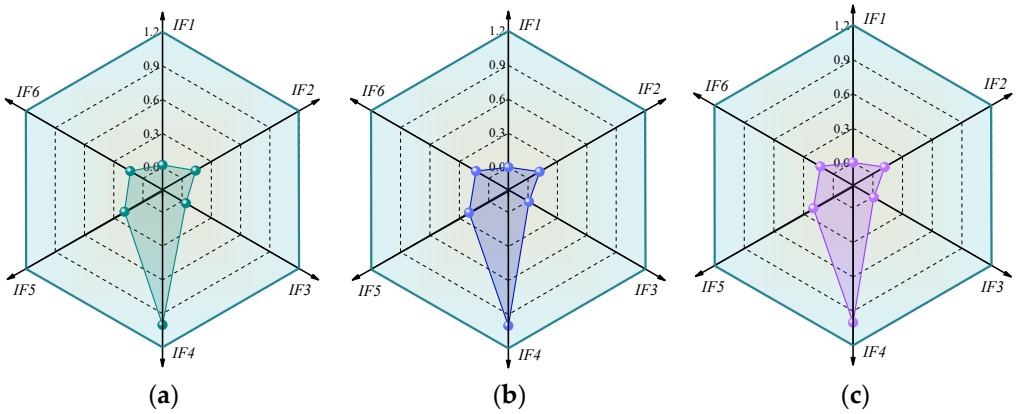


Figure 12. Range analysis of three power parameters: (**a**–**c**) the coefficients η_1, η_2, and φ. Note: *IF1–IF6* are the explosive equivalent (W), room length (R), venting coefficient $(S/V^{2/3})$, number of propagation rooms (n), strength (σ) and thickness (H) of masonry walls, respectively.

Analysis of variance (ANOVA) is employed to quantitatively evaluate the statistical significance of the influence of each factor on the blast-effect parameters by calculating the F value [33]. The F values are determined according to Equations (5)–(7), and the corresponding results are summarized in Table 5. It can be observed that the main effects of the TNT equivalent, room size, venting coefficient, wall strength, and wall thickness on the attenuation coefficients of peak overpressure, equivalent duration, and wall center ejection velocity do not reach statistical significance $(p > 0.05)$, indicating that these factors exert negligible influence on the attenuation of blast effects. By marked contrast, the number of propagation rooms exerts a highly significant influence on all three attenuation coefficients $(p < 0.001)$ and is therefore identified as the dominant factor governing the attenuation of blast effects.

$$F = (SSB \cdot DFE)/(SSE \cdot DFB) \tag{5}$$

$$SSB = \sum_{i=1}^{L} \left(\overline{y}_{\mathrm{i}} - \overline{y}\right)^2 \tag{6}$$

$$SSE = \sum_{i=1}^{N} \left(y_{\mathrm{i}} - \overline{y}\right)^2 - \sum_{i=1}^{L} \left(\overline{y}_{\mathrm{i}} - \overline{y}\right)^2 \tag{7}$$

where SSB is the between-group sum of squares; SSE is the within-group sum of squares; y_{i} is the i-th experimental result; $\overline{y}_{\mathrm{i}}$ is the average value of experimental results of the i-th level; $\overline{y}$ is the average value of all experimental results; DFE is the within-group degrees of freedom; DFB is the between-group degrees of freedom; L is the number of factor levels.

In summary, the number of propagation rooms constitutes a critical factor influencing both horizontal blast wave propagation and the ejection velocity of wall fragments in RC frame structures. Furthermore, comparative analysis demonstrates that enhancing the strength and thickness of masonry walls provides superior blast resistance compared to modifying room dimensions or venting coefficients.

Table 5. Analysis of variance.

Parameters	*SSB*	*DOF*	*F*	*p*	Significance
Attenuation coefficients of peak overpressure					
IF1	0.000	4	0.445	0.774	Not significant
IF2	0.000	3	0.422	0.748	Not significant
IF3	0.000	4	0.190	0.932	Not significant
IF4	3.563	4	3647	<0.001	Significant
IF5	0.000	3	0.017	0.996	Not significant
IF6	0.000	2	0.104	0.904	Not significant
SSE	0.001	4	/	/	/
Attenuation coefficients of equivalent duration					
IF1	0.001	4	0.433	0.781	Not significant
IF2	0.004	3	1.692	0.305	Not significant
IF3	0.005	4	1.458	0.362	Not significant
IF4	3.330	4	1077	<0.001	Significant
IF5	0.001	3	0.597	0.650	Not significant
IF6	0.002	2	1.022	0.438	Not significant
SSE	0.003	4	/	/	/
Attenuation coefficients of ejection velocity at the wall center					
IF1	0.014	4	0.524	0.727	Not significant
IF2	0.019	3	0.925	0.506	Not significant
IF3	0.008	4	0.297	0.867	Not significant
IF4	2.664	4	98.22	<0.001	Significant
IF5	0.014	3	0.674	0.612	Not significant
IF6	0.009	2	0.682	0.556	Not significant
SSE	0.027	4	/	/	/

Note: *SSB* denotes between-group sum of squares; *DOF* denotes degrees of freedom; *F* represents the *F* value, which is defined as the ratio of between-group mean square to error mean square; *SSE* is the within-group sum of squares.

4.3. Prediction Model

Given that the power parameters propagated to adjacent rooms are influenced by a multitude of factors, the simulation data are complex and show strong non-linear characteristics. Traditional fitting methods, such as linear regression and polynomial fitting, are prone to overfitting and struggle to handle high-dimensional data [34]. Among various artificial intelligence and neural network algorithms, the BP neural network is capable of deeply mining, identifying, and learning multi-dimensional non-linear relationships embedded in large datasets [35]. Therefore, in this section, a BP neural network was employed to establish a rapid prediction model for the attenuation coefficients of power parameters (η_1, η_2, and φ), incorporating structural parameters, explosive characteristics, and the number of propagation rooms as key inputs.

A BP neural network prediction model was developed, as shown in Figure 13. The dataset was partitioned in a group-based manner according to the 25 simulation cases, such that all samples originating from the same simulation case were assigned to the same set. The training set comprised 85% of the samples, and the remaining 15% served as an independent test set used exclusively to verify the accuracy and reliability of the prediction model. The prediction performance of the neural network was evaluated using the mean squared error (MSE) and the coefficient of determination (R^2), as shown in Equations (8) and (9).

$$MSE = \frac{1}{N}\sum_{i-1}^{N}(x_i - \widehat{x}_i)^2 \quad (8)$$

$$R^2 = 1 - \frac{\sum_{i=1}^{N} (x_i - \widehat{x}_i)^2}{\sum_{i=1}^{N} (x_i - \overline{x}_i)^2} \quad (9)$$

where x_i is the test data; $\widehat{x}_i$ is the predicted results; $\overline{x}_i$ is the average of all test datasets.

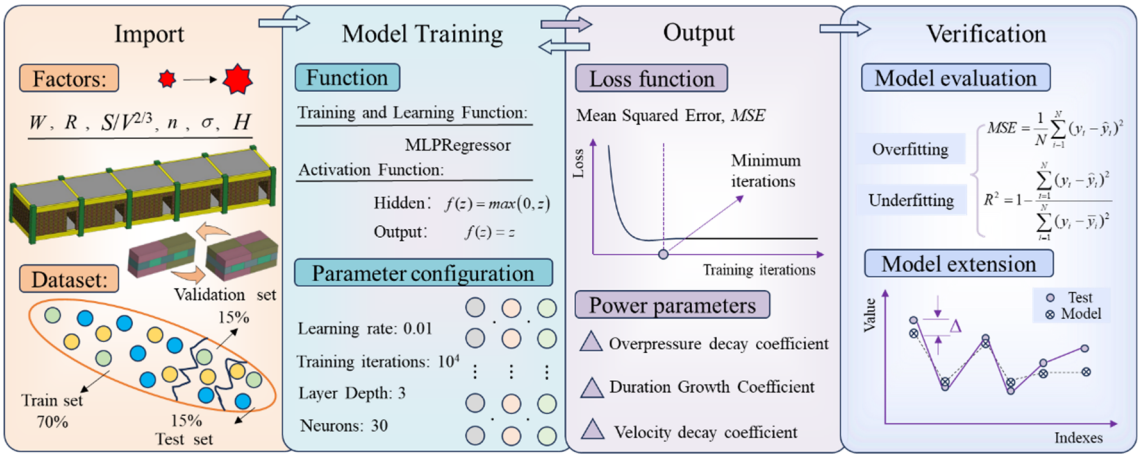


Figure 13. Prediction model and algorithm workflow based on BP neural network.

As shown in Table 6, we adopted a grid search strategy coupled with five-fold cross-validation to optimize the hyperparameters of the model, which include the number of hidden layers, the number of neurons, and the activation function. Table 7 further reports the representative search results for the single hidden layer configuration, summarizing the average values of R^2 and MSE for both the training set and the validation set. The results indicate that as the number of neurons in the hidden layer increases, the performance metrics on the training set improve continuously and gradually approach convergence, while the performance metrics on the validation set demonstrate a clear trend of increasing first and then decreasing. Among all the tested candidate configurations, the 6-36-3 network architecture delivers the optimal performance on the validation set. Accordingly, this network architecture is selected for this study.

Table 6. Hyperparameter search space and optimal parameters.

Hyperparameter	Search Space	Search Strategy	Optimal Value
Number of hidden layers	[1, 2]	Integer search	1
Number of neurons	[4, 64] Step = 4	Power-law search	36
Activation function	[Tanh, ReLU, Sigmoid]	Exhaustive search	Tanh
Number of epochs	[50, 500] Step = 50	Integer search	350
Optimizer	Adam	-	Adam

Table 7. Representative search results for the single hidden layer configuration.

Network Architecture	R^2 (Training Set)	MSE (Training Set)	R^2 (Validation Set)	MSE (Validation Set)
6-4-3	0.84	0.027	0.82	0.031
6-12-3	0.89	0.018	0.87	0.022
6-16-3	0.91	0.013	0.90	0.015
6-20-3	0.94	0.0091	0.92	0.011

Table 7. *Cont.*

Network Architecture	R^2 (Training Set)	MSE (Training Set)	R^2 (Validation Set)	MSE (Validation Set)
6-28-3	0.96	0.0048	0.95	0.0062
6-36-3	0.98	0.0018	0.97	0.0035
6-40-3	0.99	0.0013	0.97	0.0042
6-48-3	0.98	0.0017	0.96	0.0058
6-56-3	0.99	0.0009	0.97	0.0054
6-64-3	0.99	0.0015	0.95	0.0061

Figure 14 shows the test dataset and predicted results for three attenuation coefficients of power parameters. It can be seen that the BP neural network-based prediction model exhibits strong fitting performance, with errors below 20%. This indicates the prediction model successfully avoids overfitting while maintaining good generalization capability.

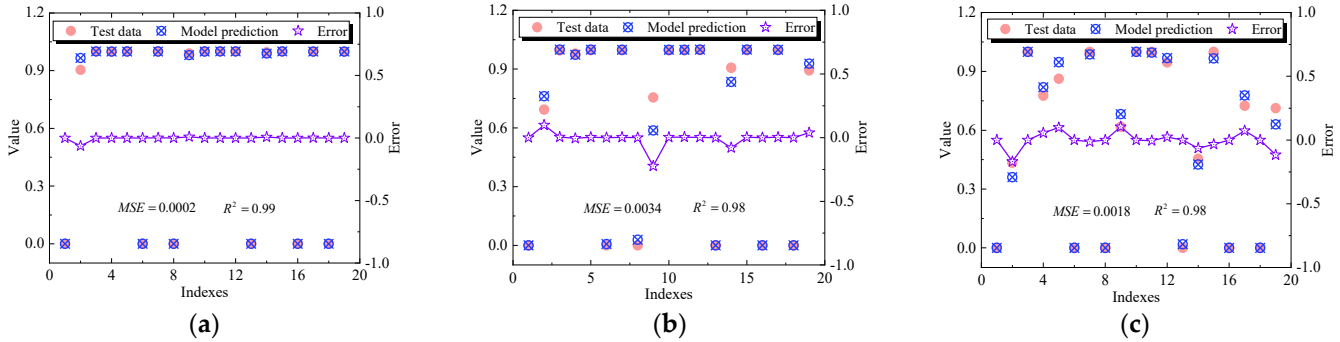


Figure 14. Test dataset and predicted results for attenuation coefficients of power parameters: (**a**–**c**) the coefficients η_1, η_2, and φ.

5. Conclusions

Based on the validated FE modeling and analysis approach for internal explosions in RC frame structures, the blast wave and the ejection velocity of wall fragments propagated to adjacent rooms were analyzed. Additionally, orthogonal tests and BP neural networks were employed to develop prediction models for the attenuation coefficient of power parameters. The main conclusions are summarized as follows:

(i) Blast damage assessment for masonry walls (WX-type walls) along the propagation direction of shock waves needs to consider both the shock waves and explosive ejection of wall fragments from the explosive source room, which can be characterized by the ejection velocity of the wall center. For other walls (WY-type walls), the damage depends solely on shock waves, which can be characterized by the peak overpressure and equivalent duration at the wall center.

(ii) Along the horizontal direction in the single-story multi-room RC frame, the shock wave loads propagated to adjacent rooms are reduced by approximately two orders of magnitude for peak overpressure and one order of magnitude for impulse compared with the preceding room. Furthermore, the kinetic energy of WX-type walls decreases approximately exponentially with an increase in the number of propagation rooms.

(iii) The number of propagation rooms is the primary factor influencing the attenuation coefficients of power parameters propagated to adjacent rooms, followed by the strength and thickness of masonry walls. The least influential factors are the room dimensions, venting coefficient, and explosive equivalent. Given a fixed number of propagation rooms, increasing the strength and thickness of masonry walls can effectively improve the blast resistance of RC frame structures.

(iv) The developed BP neural network model can accurately predict the attenuation coefficients of peak overpressure, equivalent duration, and the ejection velocity of wall fragments under different structural parameters, explosive equivalent, and number of propagation rooms. The model exhibits strong generalization performance with prediction errors below 20%.

The present study investigates the propagation characteristics of blast waves in a typical single-story, multi-room RC frame structure. Nevertheless, when extending the methodology established in this work to multi-story structural systems, several additional critical factors should be considered, such as the variation of wall bearing capacity under vertical loads and the pressure relief paths between floors. These aspects will be further investigated in our future work.

Author Contributions: Conceptualization, T.Q. and J.L.; methodology, T.Q.; software, T.Q.; validation, T.Q.; formal analysis, T.Q.; investigation, T.Q.; resources, J.L.; data curation, T.Q.; writing—original draft preparation, T.Q.; writing—review and editing, T.Q. and J.L.; visualization, T.Q.; supervision, J.L.; project administration, J.L.; funding acquisition, J.L. All authors have read and agreed to the published version of the manuscript.

Funding: This research was funded by the National Funded Postdoctoral Research Program (No. GZB20250755).

Data Availability Statement: The original contributions presented in this study are included in the article. For further inquiries, please contact the corresponding author.

Acknowledgments: The authors would like to acknowledge the financial support from the National Funded Postdoctoral Research Program (No. GZB20250755).

Conflicts of Interest: The authors declare no conflicts of interest.

References

1. Turan, A.İ.; Ayaz, Y.; Yalciner, H.; Kumbasaroglu, A. An experimental evaluation on structural performance level of corroded reinforced concrete frames. *Eng. Struct.* **2025**, *325*, 119479. [CrossRef]
2. Wang, S.; Cheng, X.; Li, Y.; Yang, X.; Zhang, H.; Guo, R.; Song, X.; Liang, Z. Assessing progressive collapse regions of reinforced concrete frame structures using graph convolutional networks. *Eng. Struct.* **2025**, *322*, 119076. [CrossRef]
3. Russia's Precision Strike Wipes Out Ukrainian Military Command Center-Top Brass. Available online: https://tass.com/defense/1628595/amp (accessed on 16 September 2026).
4. Fatima, A.; Sangi, A.J.; Mohammad, A.F.; Joohi, M. Global response of reinforced concrete framed building under varying blast load pulse shapes. *Structures* **2023**, *50*, 482–493. [CrossRef]
5. Zhang, X.-L.; Jia, D.-W.; Wang, S.-L.; Wan, Z.-Q.; Wu, Z.-Y. Analysis of structural collapse fragility based on cost-sensitive neural network under blast load. *Structures* **2025**, *71*, 107927. [CrossRef]
6. To, Q.B.; Shin, J.; Kim, J.; Han, S.W.; Lee, K. Finite element analysis-based blast and seismic performance evaluation for RC frame with retrofitted ENTA damper systems. *Eng. Struct.* **2024**, *313*, 118300. [CrossRef]
7. Kim, H.J.; Hwang, K.; Yoon, Y.H.; Lee, H.-J. Numerical analysis of the effect of afterburning on damage to the concrete structure under interior explosion. *Int. J. Concr. Struct. Mater.* **2022**, *16*, 6. [CrossRef]
8. Zhou, H.; Zheng, C.; Lu, A.; Zhu, Z.; Kong, X.; Wu, W. An experimental study of the effects of degrees of confinement on the response of thermoplastic fiber-metal laminates subjected to blast loading. *Thin-Walled Struct.* **2023**, *192*, 111125. [CrossRef]
9. Wang, Y.; Li, W.; Zhu, W.; Zhang, Q.; Li, W.; Wang, X. Dynamic response of steel cabin structure under blast loading from adjacent cabin. *Eng. Struct.* **2024**, *311*, 118213. [CrossRef]
10. Santos, A.P.; Castedo, R.; López, L.M.; Chiquito, M.; Yenes, J.I.; Alañón, A.; Costamagna, E.; Martínez-Almajano, S. Reinforced concrete building with IED detonation: Test and simulation. *Appl. Sci.* **2022**, *12*, 7803. [CrossRef]
11. López, L.M.; Pérez-Caldentey, A.; Santos, A.P.; Diego, Y.G.; Castedo, R.; Chiquito, M. Experimental response and numerical modelling of a full-scale two-span concrete slab frame subjected to blast load. *Eng. Struct.* **2023**, *296*, 116969. [CrossRef]
12. Guo, X.; Li, Y.; McCrum, D.P.; Hu, Y.; Bai, Z.; Zhang, H.; Li, Z.; Wang, X. A reinforced concrete shear wall building structure subjected to internal TNT explosions: Test results and numerical validation. *Int. J. Impact Eng.* **2024**, *190*, 104950. [CrossRef]
13. Li, X.D.; Yin, J.P.; Zhao, P.D.; Zhang, L.; Xu, Y.X.; Wang, Q.; Zhang, P. The effect of stand-off distance on damage to clamped square steel plates under enclosed explosion. *Structures* **2020**, *25*, 965–978. [CrossRef]

14. Liu, S. Study on the Distribution Range of Explosion Power Field in Frame Building Space. Ph.D. Thesis, Academy of Military Sciences, Beijing, China, 2024.
15. Lv, J.; Wu, H.; Lu, Y.; Chen, D. High-efficiency assessment method of damage for building structures under explosions. *Explos. Shock Waves* **2025**, *45*, 015101. [CrossRef]
16. Ou, Y.; Wang, F.; Wu, H.; Li, J. Damage effects of a prototype RC frame structure subjected to explosions. *Explos. Shock Waves* **2026**, *46*, 50–67. [CrossRef]
17. Chen, D.; Wu, H.; Cheng, Y. Dynamic behaviors of unreinforced and spray polyurea retrofitted brick masonry infill walls under blast loads: Shock tube test and analyses. *Int. J. Impact Eng.* **2024**, *190*, 104975. [CrossRef]
18. Lu, J.X.; Wu, H.; Chen, D. Evaluation of collapse resistance of masonry-infilled RC frame building under blast loadings. *Structures* **2023**, *50*, 1126–1146. [CrossRef]
19. Parisi, F.; Balestrieri, C.; Asprone, D. Blast resistance of tuff stone masonry walls. *Eng. Struct.* **2016**, *113*, 233–244. [CrossRef]
20. Shi, Y.; Xiong, W.; Li, Z.-X.; Xu, Q. Experimental studies on the local damage and fragments of unreinforced masonry walls under close-in explosions. *Int. J. Impact Eng.* **2016**, *90*, 122–131. [CrossRef]
21. Yu, Q.; Zeng, D.; Xu, X.; Li, S.; Dong, W.; Dai, L. Experimental and numerical investigation of polymer-reinforced and normal autoclaved aerated concrete masonry walls under large TNT explosive loads. *Int. J. Impact Eng.* **2022**, *164*, 104188. [CrossRef]
22. Keys, R.A.; Clubley, S.K. Experimental analysis of debris distribution of masonry panels subjected to long duration blast loading. *Eng. Struct.* **2017**, *130*, 229–241. [CrossRef]
23. Ciornei, L. Performance of Polyurea Retrofitted Unreinforced Concrete Masonry Walls Under Blast Loading. Master's Thesis, University of Ottawa, Ottawa, ON, Canada, 2012.
24. Edri, I.E.; Yankelevsky, D.Z.; Remennikov, A.M.; Rabinovitch, O. Combined experimental and theoretical study on the blast response of arching masonry walls. *Int. J. Impact Eng.* **2023**, *174*, 104495. [CrossRef]
25. Li, J.; Lu, Y.; Miao, H.; Xu, H.; Feng, X.; Yuan, Y. Study on Vertical Propagation of Power Parameters in RC Frame Under Internal Explosion. *Buildings* **2025**, *15*, 2080. [CrossRef]
26. *GB 50010-2010*; Code for Design of Concrete Structures. China Architecture & Building Press: Beijing, China, 2015.
27. *GB 50011-2010*; Code for Seismic Design of Buildings. China Architecture & Building Press: Beijing, China, 2016.
28. Li, J.; Wu, H.; Lu, Y. Damage assessment of prototype RC frame structure with masonry-infilled walls under external explosion: Tests and numerical simulations. *Eng. Struct.* **2026**, *369*, 123798. [CrossRef]
29. Li, J.; Lu, Y.; Feng, X.; Wu, H. Analysis of internal explosion load characteristics and dynamic behavior in RC box structures. *Explos. Shock Waves* **2026**, *46*, 013101. [CrossRef]
30. Guo, B.; Liang, W.; Xu, X.; Song, S.; Fu, Q.; Liu, S. Study on the characteristics of internal explosion loads in masonry-infilled reinforced concrete frame structures. *J. Build. Eng.* **2025**, *111*, 113243. [CrossRef]
31. *UFC 3-340-02*; Structures to Resist the Effects of Accidental Explosions. U.S. Department of Defense: Washington, DC, USA, 2008.
32. Wei, Y.; Li, L.; Li, Z.; Liu, S. Preparation of vegetative concrete with recycled aggregate: Mix proportion orthogonal test, curing methods, and microstructure. *Constr. Build. Mater.* **2025**, *460*, 139892. [CrossRef]
33. Li, Y.; Zhang, H.; Fang, Q.; Yu, T.; Yang, J.; Li, W. Optimization of mechanical properties and water resistance of sawdust-magnesium oxychloride cement composites based on orthogonal tests. *Constr. Build. Mater.* **2024**, *439*, 137300. [CrossRef]
34. Ning, J.; Feng, Y.; Ren, H.; Xu, X. Prediction model for the failure behavior of concrete under impact loading based on back propagation neural network. *Constr. Build. Mater.* **2024**, *411*, 134297. [CrossRef]
35. Xiao, R.; Liu, W.; Kong, D. Failure criterion and seismic fragility evaluation of isolated nuclear power plant piping system using BP neural network. *Eng. Fail. Anal.* **2024**, *165*, 108790. [CrossRef]

Disclaimer/Publisher's Note: The statements, opinions and data contained in all publications are solely those of the individual author(s) and contributor(s) and not of MDPI and/or the editor(s). MDPI and/or the editor(s) disclaim responsibility for any injury to people or property resulting from any ideas, methods, instructions or products referred to in the content.